Multi-layered Elastic Analysis Formulation for Surface Moment Loading

James W. Maina
CSIR
P O Box 395
Pretoria 0001, South Africa
Tel.: +27-12-841-3956
Fax: +27-12-841-3232
JMaina@csir.co.za

Kiyoshi Fujinami
Research Associate
Dept. of Civil and Environmental Engineering, Tokyo Denki University
Hatoyama-Cho, Hiki-Gun, Saitama 350-0394, JAPAN
Tel.: +81-492-96-2911
Fax: +81-492-96-6501
fkiyo@g.dendai.ac.jp

Kunihito Matsui
Professor
Dept. of Civil and Environmental Engineering, Tokyo Denki University
Hatoyama-Cho, Hiki-Gun, Saitama 350-0394, JAPAN
Tel.: +81-492-96-2911
Fax: +81-492-96-6501
matsui@g.dendai.ac.jp

Takemi Inoue
Executive Managing Director
NIPPO Corporation
19-11 Kyobashi 1-Chome. Chuo-Ku, Tokyo 104-8380, JAPAN
Tel.: +81-3-3563-6760
Fax: +81-3-3567-4575
inoue_takemi@nippo-c.jp, takemii@mb.infoweb.ne.jp

TOTAL NUMBER OF WORDS (including abstract, figures and tables): 6,746

ABSTRACT

When pavement structures like roads and runways are under simultaneous actions of vehicular vertical and horizontal wheel loading, analysis is normally performed considering these loads as uniformly distributed vertical and horizontal loads, respectively. Measurements by Stress-In-Motion (SIM) technology on slow (creep) speed truck tires have shown that, depending on the magnitude of the load, there are acceptable "n" or unacceptable "m" shaped stress distributions at the tire/road interface. In order for accurate mathematical derivation of, for example, non-uniform "m" shaped surface stress to be performed, authors have proposed introduction of a moment-like surface loading. Detailed derivation of closed form solutions of pavement responses due to the action of non-uniform circular loading is presented in this paper. Results show that maximum compressive stress at the pavement surface due to triangular load was greater by 20% and 70% than results from uniformly distributed vertical load and horizontal load, respectively. Moreover, there was an increase of more than 60% in tensile strain at the bottom of the asphalt layer, ε_x, and compressive strain, ε_z, at the top of subgrade layer for triangular load as compared to uniformly distributed load. Planned future publications will use results from SIM measurements and look at practical implications of this type of non-uniform loading on performance of different types of pavement structures.

INTRODUCTION

Revision of the Japanese Guide for Pavement Structures in April, 2001 was followed by the publications of the Technical Standards for Pavement Structures and its Commentary that were published by the Japan Road Association under the auspices of the Ministry of Land, Infrastructure and Transport. Publication of these documents has paved the way for application of performance specification as well as mechanistic-empirical methods to pavement design. One of the requisite for performance specification is the computation of fatigue failure, which would involve software development and material modeling for proper pavement analysis.

In 1997, the General Accounting Office (GAO) published a challenging report that the AASHTO pavement design guide was outdated and recommended the use of (nonlinear) three dimensional finite element methods (3D-FEM) for analysis and evaluation of pavement structures *(1)*. Several 3D-FEM related symposiums have since then been organized in USA as well as Europe (*2*, *3,4*). More recently, AASHTO sponsored development of mechanistic-empirical pavement design guide (*5*). Despite of the advantages offered by 3D-FEM software (*6*) (ABAQUS, ANSYS, MARC, NASTRAN, etc) like handling of complex surface loading patterns, various material properties and environmental conditions, substantial experience that is required for one to use 3D-FEM and obtain good results is a major hindrance to wider use of this technique. FEM software tailored specifically for pavement problems like MICHPAVE (ILLI-PAVE) developed in the US or PAVE3D developed in Japan (7) may help reduce problems introduced by the general FEM packages. However, user friendliness and computational capabilities need to be improved for wider acceptance and use. Alternatively, methods based on improved multilayered linear elastic analysis are still practical means of evaluating and analyzing pavement structures.

Software like BISAR, CHEVRON and ELSA that were developed based on classic elastic theory are widely used in Japan and many parts of the world. Moreover, authors of this paper developed GAMES software with functional capabilities similar to BISAR (*8*, *9*). The GAMES software was also developed based on the theory of elasticity and its graphical user interface does not require a skilled user for its proper operation.

CHEVRON and ELSA were developed mainly for the analysis based on vertical surface load only while BISAR and GAMES are capable of considering among other things, vertical as well as horizontal surface loading together with layer interface slip (*10*). In all these software, the load must be uniformly distributed circular load. The surface vertical load is from the wheel load while the surface horizontal load is the result of the force exerted on the pavement surface due to starting/stopping of a vehicle.

The fact that cause of pavement surface distresses like cracking, spalling, distortion, surface particle disintegration and surface heaving on very specific pavement sections like road intersections, highway exits and airport pavements at landing and takeoff sections can not completely be explained by the actions of uniformly distributed vertical and horizontal load only requires more types of pavement loading to be considered. Results of measured Stress-In-Motion (SIM) data presented by De Beer et. al (*11*, *12*) show two types of contact stresses depending on the loading condition. The first type is the acceptable “n-shape” stress distribution, which is a relatively uniform concave bulge. The second type is the unacceptable “m-shape” stress distribution, which represents over-loading where two distinctive convex like peak stresses occur at the tire edges.

In recent improvements of the GAMES software, torsional surface loading that is exerted on the pavement surface when large-sized vehicles like trucks and trailers take, particularly, sharp corners was added on the list of loading types that can be considered for

analysis (*13*). Further improvement is suggested whereby an introduction of a moment-like surface loading to the derivation of closed form solution of pavement responses will help develop contact surface stresses similar to such types as, for example, contact stresses measured by SIM technology.

This paper reports on the continuing efforts to improve computational capabilities of the GAMES software by presenting the formulation, together with worked examples, for pavement analysis that takes into consideration surface moment loading.

GOVERNING EQUATIONS

The governing equations may be presented by using cylindrical coordinate system and assume that a circular load, with radius a, is acting on the pavement surface and the magnitude of the load varies linearly (see Figures 1-4). Global and local Cartesian coordinate systems are used, thereafter, for proper referencing of the positions of the load and points of interest.

The vertical load, p, at the surface ($z = 0$) may be represented in cylindrical coordinates as:

$$p = p_0 + p_1 \frac{r\cos\theta}{a} \quad (0 \le r \le a) \tag{1a}$$

$$p = 0 \quad (r > a) \tag{1b}$$

Furthermore, the horizontal load q, may be given in cylindrical coordinates as:

$$q = q_0 + q_1 \frac{r\cos\theta}{a} \quad (0 \le r \le a) \tag{2a}$$

$$q = 0 \quad (r > a) \tag{2b}$$

The first item, p_0, on the right hand side of Equation (1a) is the uniformly distributed vertical load, while the second item represents the load, which is anti-symmetric about the y-axis. The loading distribution obtained from Equation (1a) is a sum of uniformly distributed load and the load that is anti-symmetric about y-axis. All the loads in Equation (1a) are symmetric about x-axis. In this research, the anti-symmetric load obtained is known as moment load. The trapezoidal load that results from the combination of uniformly distributed load, p_0 and anti-symmetric load p_1 is as shown in Figure 2. The positive z-axis is considered to point downward. In this regard, the boundary condition at the surface of the pavement can be represented in cylindrical coordinates as follows:

$$\sigma_z(r,0) = \begin{cases} -p_0 & (0 \le r \le a) \\ 0 & (r > a) \end{cases} \tag{3}$$

$$\frac{\sigma_z(r,0)}{\cos\theta} = \begin{cases} -p_1\left(\frac{r}{a}\right) & (0 \le r \le a) \\ 0 & (r > a) \end{cases} \tag{4}$$

Sum of the uniformly distributed horizontal load, q_0, and anti-symmetric load, q_1, in case of horizontal surface loading may similarly be considered. Boundary conditions for the uniformly distributed horizontal load may be given as:

$$\tau_{zr}(r,0) = -q_0 \cos\theta \tag{5a}$$

$$\tau_{z\theta}(r,0) = q_0 \sin\theta \tag{5b}$$

which yield:

$$\frac{\tau_{z\theta}(r,0)}{\cos\theta} - \frac{\tau_{zr}(r,0)}{\sin\theta} = \begin{cases} 2q_0 & (0 \le r \le a) \\ 0 & (r > a) \end{cases} \tag{6a}$$

$$\frac{\tau_{z\theta}(r,0)}{\cos\theta} + \frac{\tau_{zr}(r,0)}{\sin\theta} = 0 \quad (r \ge 0) \tag{6b}$$

Furthermore, boundary conditions for the anti-symmetric distributed horizontal load may be given as:

$$\tau_{zr}(r,0) = -q_1 \left(\frac{r}{a}\right) \cos^2\theta \tag{7a}$$

$$\tau_{z\theta}(r,0) = q_1 \left(\frac{r}{a}\right) \cos\theta \sin\theta \tag{7b}$$

which yield:

$$\frac{\tau_{z\theta}(r,0)}{\cos\theta} - \frac{\tau_{zr}(r,0)}{\sin\theta} = \begin{cases} 2q_1 \left(\frac{r}{a}\right) \cos\theta & (0 \le r \le a) \\ 0 & (r > a) \end{cases} \tag{8a}$$

$$\frac{\tau_{z\theta}(r,0)}{\cos\theta} + \frac{\tau_{zr}(r,0)}{\sin\theta} = 0 \quad (r \ge 0) \tag{8b}$$

Consider local Cartesian coordinates (x, y, z) and local cylindrical coordinates (r, θ, z) to have the same point of origin where the angle between r-axis and x-axis is θ. Furthermore, assume that the center of the circular load is the origin of the local coordinate system and the direction of horizontal load to be the same as positive x-axis of the local coordinate system. By introducing the local cylindrical coordinates (r, θ, z) with same z-axis as the local Cartesian coordinates, the equilibrium equations may be expressed in terms of Navier equations as follows:

$$\nabla^2 u_r + \frac{1}{1-2\nu} \frac{\partial}{\partial r} \left(\frac{\partial u_r}{\partial r} + \frac{u_r}{r} + \frac{1}{r} \frac{\partial u_\theta}{\partial \theta} + \frac{\partial u_z}{\partial z} \right) - \frac{u_r}{r^2} - \frac{2}{r^2} \frac{\partial u_\theta}{\partial \theta} = 0 \tag{9a}$$

$$\nabla^2 u_\theta + \frac{1}{1-2\nu} \frac{1}{r} \frac{\partial}{\partial \theta} \left(\frac{\partial u_r}{\partial r} + \frac{u_r}{r} + \frac{1}{r} \frac{\partial u_\theta}{\partial \theta} + \frac{\partial u_z}{\partial z} \right) - \frac{u_\theta}{r^2} + \frac{2}{r^2} \frac{\partial u_r}{\partial \theta} = 0 \tag{9b}$$

$$\nabla^2 u_z + \frac{1}{1-2\nu} \frac{\partial}{\partial z} \left(\frac{\partial u_r}{\partial r} + \frac{u_r}{r} + \frac{1}{r} \frac{\partial u_\theta}{\partial \theta} + \frac{\partial u_z}{\partial z} \right) = 0 \tag{9c}$$

where, ν is the Poisson's ratio, u_r, u_θ, u_z are cylindrical displacements in the r, θ, z directions, respectively. Moreover, the Laplace operator, ∇^2, in the cylindrical coordinate system may be given as:

$$\nabla^2 = \frac{\partial^2}{\partial r^2} + \frac{1}{r}\frac{\partial}{\partial r} + \frac{1}{r^2}\frac{\partial^2}{\partial \theta^2} + \frac{\partial^2}{\partial z^2} \tag{10}$$

The stress may be expressed in terms of displacements as shown in the following equations:

$$\sigma_r = (\lambda + 2\mu)\frac{\partial u_r}{\partial r} + \lambda\left(\frac{u_r}{r} + \frac{1}{r}\frac{\partial u_\theta}{\partial \theta} + \frac{\partial u_z}{\partial z}\right) \tag{11a}$$

$$\sigma_\theta = (\lambda + 2\mu)\left(\frac{u_r}{r} + \frac{1}{r}\frac{\partial u_\theta}{\partial \theta}\right) + \lambda\left(\frac{\partial u_r}{\partial r} + \frac{\partial u_z}{\partial z}\right) \tag{11b}$$

$$\sigma_z = (\lambda + 2\mu)\frac{\partial u_z}{\partial z} + \lambda\left(\frac{\partial u_r}{\partial r} + \frac{u_r}{r} + \frac{1}{r}\frac{\partial u_\theta}{\partial \theta}\right) \tag{11c}$$

$$\tau_{\theta z} = \mu\left(\frac{\partial u_\theta}{\partial z} + \frac{1}{r}\frac{\partial u_z}{\partial \theta}\right) \tag{11d}$$

$$\tau_{rz} = \mu\left(\frac{\partial u_r}{\partial z} + \frac{1}{r}\frac{\partial u_z}{\partial r}\right) \tag{11e}$$

$$\tau_{r\theta} = \mu\left(\frac{1}{r}\frac{\partial u_r}{\partial \theta} + \frac{\partial u_\theta}{\partial r} - \frac{u_\theta}{r}\right) \tag{11f}$$

where, λ and μ are Lame's constants, which are related in the following manner:

$$\lambda = \frac{2\nu}{1-2\nu}\mu \tag{11g}$$

SOLUTION FOR THE GOVERNING EQUATIONS

The governing equations presented in the previous sections may be solved by using of the Michell function $\Phi(r, \theta, z)$ and Boussinesq function $\Psi(r, \theta, z)$. Using these functions, displacement in the cylindrical coordinate system may be written as:

$$u_r = -\frac{\partial^2 \Phi}{\partial r \partial z} + \frac{2}{r}\frac{\partial \Psi}{\partial \theta} \tag{12a}$$

$$u_\theta = -\frac{1}{r}\frac{\partial^2 \Phi}{\partial \theta \partial z} - 2\frac{\partial \Psi}{\partial r} \tag{12b}$$

$$u_z = 2(1-\nu)\nabla^2 \Phi - \frac{\partial^2 \Phi}{\partial z^2} \tag{12c}$$

Substituting Equation (12) into Equation (11) and rearrange:

$$\frac{\sigma_r}{2\mu} = \frac{\partial}{\partial z}\left(\nu\nabla^2 - \frac{\partial^2}{\partial r^2}\right)\Phi - 2\frac{\partial}{\partial \theta}\left(\frac{1}{r^2} - \frac{1}{r}\frac{\partial}{\partial r}\right)\Psi \tag{13a}$$

$$\frac{\sigma_\theta}{2\mu} = \frac{\partial}{\partial z}\left(\nu\nabla^2 - \frac{1}{r}\frac{\partial}{\partial r} - \frac{1}{r^2}\frac{\partial^2}{\partial \theta^2}\right)\Phi + 2\frac{\partial}{\partial \theta}\left(\frac{1}{r^2} - \frac{1}{r}\frac{\partial}{\partial r}\right)\Psi \tag{13b}$$

$$\frac{\sigma_z}{2\mu} = \frac{\partial}{\partial z}\left((2-\nu)\nabla^2 - \frac{\partial^2}{\partial z^2}\right)\Phi \tag{13c}$$

$$\frac{\tau_{\theta z}}{2\mu} = \frac{1}{r}\frac{\partial}{\partial \theta}\left((1-\nu)\nabla^2 - \frac{\partial^2}{\partial z^2}\right)\Phi - \frac{\partial^2}{\partial r \partial z}\Psi \tag{13d}$$

$$\frac{\tau_{zr}}{2\mu} = \frac{\partial}{\partial r}\left((1-\nu)\nabla^2 - \frac{\partial^2}{\partial z^2}\right)\Phi + \left(\frac{1}{r}\frac{\partial^2}{\partial \theta \partial z}\right)\Psi \tag{13e}$$

$$\frac{\tau_{r\theta}}{2\mu} = \frac{1}{r}\frac{\partial^2}{\partial z \partial \theta}\left(\frac{1}{r} - \frac{\partial}{\partial r}\right)\Phi + \left(\frac{1}{r^2}\frac{\partial^2}{\partial \theta^2} - \frac{\partial^2}{\partial r^2} + \frac{1}{r}\frac{\partial}{\partial r}\right)\Psi \tag{13f}$$

where, μ is the shear modulus of elasticity.

Substituting Equation (12) into Equation (9) and rearrange:

$$\nabla^4 \Phi = 0 \tag{14a}$$

$$\nabla^2 \Psi = 0 \tag{14b}$$

where Φ and Ψ are solutions of the biharmonic function and harmonic function, respectively.

Four types of loads are used to derive boundary conditions for Equations (1) and (2). Furthermore, based on the principle of superposition, results of responses from the individual loads may be added to obtain the general solutions for the total loads. Looking at Equation (1a), it is clear that the first load component on the right hand side of the equation is an axi-symmetric load that is independent of the variable θ. However, since the other load component in this equation is a function of θ, as explained in Reference *8*, Michell and Boussinesq functions may be re-written as:

$$\Phi(r, \theta, z) = \phi(r, z)\cos\theta \tag{15a}$$

$$\Psi(r, \theta, z) = \psi(r, z)\sin\theta \tag{15b}$$

Substituting Equation (15) into Equation (14) yields:

$$\overline{\nabla}^4 \varphi(r, z) = 0 \tag{16a}$$

$$\overline{\nabla}^2 \psi(r, z) = 0 \tag{16b}$$

where,

$$\overline{\nabla}^2 = \frac{\partial^2}{\partial r^2} + \frac{1}{r}\frac{\partial}{\partial r} - \frac{1}{r^2} + \frac{\partial^2}{\partial z^2} \tag{16c}$$

$\phi(r,z)$ and $\psi(r,z)$ are solutions for biharmonic and harmonic functions in $r-z$ coordinate axes.

Equation (17) is the result of Hankel transforms on Equation (16):

$$\left(\frac{d^2}{dz^2} - \xi^2\right)^2 G(\xi,z) = 0 \tag{17a}$$

$$\left(\frac{d^2}{dz^2} - \xi^2\right) H(\xi,z) = 0 \tag{17b}$$

where,

$$G(\xi,z) = \int_0^\infty r\phi(r,z)\, J_1(\xi r)dr \tag{18a}$$

$$H(\xi,z) = \int_0^\infty r\psi(r,z)\, J_1(\xi r)dr \tag{18b}$$

Solving Equation (17) will result in Equation (19) as follows:

$$G(\xi,z) = (A + Bz)e^{\xi z} + (C + Dz)e^{-\xi z} \tag{19a}$$

$$H(\xi,z) = Ee^{\xi z} + Fe^{-\xi z} \tag{19b}$$

where, ξ is Hankel parameter while coefficients A, B, C, D, E, F are constants of integration, which may be determined based on the boundary conditions of the problem to be solved.

In order to obtain solutions for all the responses resulting from application of the load at the surface of the pavement, the following functions were derived for the purpose of Hankel transforms:

$$H_1(\xi,z) = \int_0^\infty r\left(\frac{u_r}{\cos\theta} + \frac{u_\theta}{\sin\theta}\right) J_2(\xi r)dr \tag{20a}$$

$$H_2(\xi,z) = \int_0^\infty r\left(\frac{u_r}{\cos\theta} - \frac{u_\theta}{\sin\theta}\right) J_0(\xi r)dr \tag{20b}$$

$$H_3(\xi,z) = \int_0^\infty r\left(\frac{u_z}{\cos\theta}\right) J_1(\xi r)dr \tag{20c}$$

$$H_4(\xi,z) = \int_0^\infty r\left(\frac{\sigma_z}{\cos\theta}\right) J_1(\xi r)dr \tag{20d}$$

$$H_5(\xi,z) = \int_0^\infty r\left(\frac{\tau_{\theta z}}{\sin\theta} + \frac{\tau_{zr}}{\cos\theta}\right) J_2(\xi r)dr \tag{20e}$$

$$H_6(\xi,z)=\int_0^\infty r\left(\frac{\tau_{\theta z}}{\sin\theta}-\frac{\tau_{zr}}{\cos\theta}\right)J_0(\xi r)dr \tag{20f}$$

$$H_7(\xi,z)=\int_0^\infty r\left(\frac{\sigma_r}{\cos\theta}+\frac{1}{r}\frac{2\mu u_r}{\cos\theta}+\frac{1}{r}\frac{2\mu u_\theta}{\sin\theta}\right)J_1(\xi r)dr \tag{20g}$$

$$H_8(\xi,z)=\int_0^\infty r\left(\frac{\sigma_r}{\cos\theta}+\frac{\sigma_\theta}{\cos\theta}\right)J_1(\xi r)dr \tag{20h}$$

$$H_9(\xi,z)=\int_0^\infty r\left(\frac{\tau_{r\theta}}{\sin\theta}+\frac{1}{r}\frac{2\mu u_r}{\cos\theta}+\frac{1}{r}\frac{2\mu u_\theta}{\sin\theta}\right)J_1(\xi r)dr \tag{20i}$$

where, $J_n(\xi r)$ $(n=0,1,2)$ is the Bessel function of first kind of n^{th} order. Substituting Equation (15) into Equation (13) followed by substitution into Equations (20a) ~ (20f) and rearrange will result in Equation (21a) as follows:

$$\begin{Bmatrix}H_1(\xi,z)\\H_2(\xi,z)\\H_3(\xi,z)\\H_4(\xi,z)\\H_5(\xi,z)\\H_6(\xi,z)\end{Bmatrix}=[P(\xi,z)]\begin{Bmatrix}A(\xi)\\B(\xi)\\C(\xi)\\D(\xi)\\E(\xi)\\F(\xi)\end{Bmatrix} \tag{21a}$$

where, $[P(\xi,z)]$ is a 6×6 matrix whose elements are as follows:

$$[P(\xi,z)]=\begin{bmatrix}
\xi^2e^{\xi z} & \xi(1+\xi z)e^{\xi z} & -\xi^2e^{-\xi z} & \xi(1-\xi z)e^{-\xi z} & 2\xi e^{\xi z} & 2\xi e^{-\xi z}\\
-\xi^2e^{\xi z} & \xi(-1-\xi z)e^{\xi z} & \xi^2e^{-\xi z} & \xi(-1+\xi z)e^{-\xi z} & 2\xi e^{\xi z} & 2\xi e^{-\xi z}\\
-\xi^2e^{\xi z} & \xi(2-\xi z-4\nu)e^{\xi z} & -\xi^2e^{-\xi z} & \xi(-2-\xi z+4\nu)e^{\xi z} & 0 & 0\\
-2\mu\xi^3e^{\xi z} & 2\mu\xi^2(1-\xi z-2\nu)e^{\xi z} & 2\mu\xi^3e^{-\xi z} & 2\mu\xi^2(1+\xi z-2\nu)e^{-\xi z} & 0 & 0\\
2\mu\xi^3e^{\xi z} & 2\mu\xi^2(\xi z+2\nu)e^{\xi z} & 2\mu\xi^3e^{-\xi z} & 2\mu\xi^2(\xi z-2\nu)e^{-\xi z} & 2\mu\xi^2e^{\xi z} & -2\mu\xi^2e^{-\xi z}\\
2\mu\xi^3e^{\xi z} & 2\mu\xi^2(\xi z+2\nu)e^{\xi z} & 2\mu\xi^3e^{-\xi z} & 2\mu\xi^2(\xi z-2\nu)e^{-\xi z} & -2\mu\xi^2e^{\xi z} & 2\mu\xi^2e^{-\xi z}
\end{bmatrix}$$

Similarly for Equations (13), (15) and (20g) ~ (20i), where after rearrangement Equation (21b) would obtained as follows:

$$\begin{Bmatrix}H_7(\xi,z)\\H_8(\xi,z)\\H_9(\xi,z)\end{Bmatrix}=[Q(\xi,z)]\begin{Bmatrix}A(\xi)\\B(\xi)\\C(\xi)\\D(\xi)\\E(\xi)\\F(\xi)\end{Bmatrix} \tag{21b}$$

where, $[Q(\xi, z)]$ is a 3×6 matrix whose elements are as shown below:

$$[Q(\xi z)] = \begin{bmatrix} 2\mu\xi^3 e^{\xi z} & 2\mu\xi^2(1+\xi z+2\nu)e^{\xi z} & -2\mu\xi^3 e^{-\xi z} & 2\mu\xi^2(1-\xi z+2\nu)e^{-\xi z} & 0 & 0 \\ 2\mu\xi^3 e^{\xi z} & 2\mu\xi^2(1+\xi z+4\nu)e^{\xi z} & -2\mu\xi^3 e^{-\xi z} & 2\mu\xi^2(1-\xi z+4\nu)e^{-\xi z} & 0 & 0 \\ 0 & 0 & 0 & 0 & 2\mu\xi^2 2e^{\xi z} & 2\mu\xi^2 2e^{-\xi z} \end{bmatrix}$$

Since all responses at $z = \infty$ should converge to zero for a semi-infinite layer, coefficients in Equation (21) become:

$$A(\xi) = B(\xi) = E(\xi) = 0 \tag{22}$$

Furthermore, for purpose of simplifying computations in a multi-layered system, local coordinate system with origins at the top of each layer would be introduced. Considering compatibility of stresses and displacements at each boundary between for example, layer i and layer $i+1$, the following relationship between layers is obtained:

$$\begin{Bmatrix} H_1^{(i)}(\xi, h_i) \\ H_2^{(i)}(\xi, h_i) \\ H_3^{(i)}(\xi, h_i) \\ H_4^{(i)}(\xi, h_i) \\ H_5^{(i)}(\xi, h_i) \\ H_6^{(i)}(\xi, h_i) \end{Bmatrix} = \begin{Bmatrix} H_1^{(i+1)}(\xi, 0) \\ H_2^{(i+1)}(\xi, 0) \\ H_3^{(i+1)}(\xi, 0) \\ H_4^{(i+1)}(\xi, 0) \\ H_5^{(i+1)}(\xi, 0) \\ H_6^{(i+1)}(\xi, 0) \end{Bmatrix} \tag{23}$$

Making use of Equations (21a) and (23), relationship between constants of integration between for example layer i and layer $i+1$ may be represented as follows:

$$\begin{Bmatrix} A^{(i)}(\xi) \\ B^{(i)}(\xi) \\ C^{(i)}(\xi) \\ D^{(i)}(\xi) \\ E^{(i)}(\xi) \\ F^{(i)}(\xi) \end{Bmatrix} = \left[R^{(i)}\left(\xi, h^{(i)}\right)\right] \begin{Bmatrix} A^{(i+1)}(\xi) \\ B^{(i+1)}(\xi) \\ C^{(i+1)}(\xi) \\ D^{(i+1)}(\xi) \\ E^{(i+1)}(\xi) \\ F^{(i+1)}(\xi) \end{Bmatrix} \tag{24a}$$

where,

$$\left[R^{(i)}\left(\xi, h^{(i)}\right)\right] = \left[P^{(i)}\left(\xi, h^{(i)}\right)\right]^{-1}\left[P^{(i+1)}(\xi, 0)\right] \tag{24b}$$

Since thickness of the n^{th} layer, which is the bottom layer, is infinity, stresses and displacement at $z = \infty$ will converge to zero. This means, constant of integration for the bottom layer will be as follows:

$$A^{(n)}(\xi) = B^{(n)}(\xi) = E^{(n)}(\xi) = 0 \tag{25}$$

Making use of Equation (24) for stepwise bottom-up relationship, while taking into consideration the relationship expressed in Equation (25), the relation between stresses and displacement at the surface of layer 1 and constants of integration for the bottom layer may be expressed in terms of transfer matrix shown below:

$$\begin{Bmatrix} H_1^{(1)}(\xi,0) \\ H_2^{(1)}(\xi,0) \\ H_3^{(1)}(\xi,0) \\ H_4^{(1)}(\xi,0) \\ H_5^{(1)}(\xi,0) \\ H_6^{(1)}(\xi,0) \end{Bmatrix} = \left[P^{(1)}(\xi,0)\right]\left[R^{(1)}(\xi,h^{(1)})\right]\cdots\left[R^{(n-1)}(\xi,h^{(n-1)})\right]\begin{Bmatrix} 0 \\ 0 \\ C^{(n)}(\xi) \\ D^{(n)}(\xi) \\ 0 \\ F^{(n)}(\xi) \end{Bmatrix} \tag{26}$$

Performing Hankel transforms on the boundary conditions for surface loads expressed in Equations (1) and (2) will result in Equation (27) as shown below:

$$\tilde{p}_0(\xi) = \int_0^\infty r p_0 J_0(\xi r) dr = \frac{a p_0}{\xi} J_1(\xi a) \tag{27a}$$

$$\tilde{p}_1(\xi) = \int_0^\infty r\left(p_1 \frac{r}{a}\right) J_1(\xi r) dr = \frac{a p_1}{\xi} J_2(\xi a) \tag{27b}$$

$$2\tilde{q}_0(\xi) = \int_0^\infty r(2q_0) J_0(\xi r) dr = \frac{2aq_0}{\xi} J_1(\xi a) \tag{27c}$$

$$2\tilde{q}_1(\xi)\cos\theta = \int_0^\infty r\left(2q_1 \cos\theta \frac{r}{a}\right) J_1(\xi r) dr = \frac{q_1 \cos\theta}{\xi^2}\left[J_1(\xi a)\{2\xi a - \pi \mathbf{H}_0(\xi a)\} + \pi J_0(\xi a)\mathbf{H}_1(\xi a)\right] \tag{27d}$$

where, $\mathbf{H}_0(\xi a)$, $\mathbf{H}_1(\xi a)$ are Struve functions of orders 0 and 1 (see Appendix).

Hankel transforms of the non-uniform pavement surface loads will then become:

$$\begin{Bmatrix} H_4^{(1)}(\xi,0) \\ H_5^{(1)}(\xi,0) \\ H_6^{(1)}(\xi,0) \end{Bmatrix} = \begin{Bmatrix} \tilde{p}_1(\xi) \\ 0 \\ 2\tilde{q}_1(\xi) \end{Bmatrix} \tag{28}$$

Substitution of Equation (28) into Equation (26), constants of integrations $C^{(n)}(\xi), D^{(n)}(\xi), F^{(n)}(\xi)$ may be determined and substituting that into Equation (24) constants of integration for each layer $A^{(i)}(\xi), B^{(i)}(\xi)$ $C^{(i)}(\xi), D^{(i)}(\xi), E^{(i)}(\xi), F^{(i)}(\xi)$ may be determined in a stepwise manner. Determination of responses due to $\tilde{p}_0(\xi)$ in Equation (27a) is as explained in (*8*).

Application of Hankel transform has made it possible for the problem to be numerically quantified. Semi-infinite integration for Hankel inverse transform is performed using Double Exponential integration (*14, 15*). Improvement of the accuracy of numerical integration in the neighborhood of the pavement surface was achieved by employing Richardson extrapolation algorithm (*15*).

SEMI INFINITY SYSTEM

The principle of superposition is applied to solve for responses due to the boundary conditions expressed in Equations (1a) and (2a). The first load items in the right hand sides of Equations (1a) and (2a) represent the uniformly distributed vertical and horizontal loads whose solutions

have already been developed, checked and presented (*8*). In this section, responses due to the actions of second load items in Equations (1a) and (2a) on a semi-infinite system are presented.

The loading boundary condition in case of vertical load acting on the surface of the semi-infinite system may be expressed as follows:

$$p = p_1 \frac{r\cos\theta}{a}, \quad q = 0 \tag{29}$$

For the case of horizontal load, the loading boundary condition may be expressed as:

$$p = 0, \quad q = q_1 \frac{r\cos\theta}{a} \tag{30}$$

The boundary conditions for vertical and horizontal loads may be represented graphically as shown in Figures 3 and 4, respectively.

Dimensionless responses u_z, σ_x, τ_{xy} at the surface, where $z = 0$, for the boundary condition represented in Equation (29) were determined and presented in three dimensions as shown in Figure 5. The figure shows that, u_z is also anti-symmetric about y-axis while in the positive x-axis the deformation is downward while in the negative x-axis the deformation is upward. Correspondingly, σ_x is compressive in the positive x-axis and tensile in the negative x-axis. Moreover, when a uniformly distributed vertical load is acting, τ_{xy} is zero, but when there is an action of moment load, τ_{xy} that is symmetric about y-axis develops.

Next, dimensionless responses u_z, σ_x, τ_{xy} at the surface, where $z = 0$, for the boundary condition represented in Equation (30) were determined and presented in three dimensions as shown in Figure 6. Figure 6 shows that displacement, u_z, is symmetric about x and y-axes, zero along the y-axis and the deformation is downward on both positive and negative axes. σ_x is also symmetric about x and y-axes and zero along y-axis. With respect to the x-axis, σ_x is, to a very small extent, tensile near the origin and compressive at points far from the origin. Finally, τ_{xy}, is anti-symmetric about x and y-axes.

It is, generally, difficult to maintain high accuracy for computations of surface responses, where $z = 0$, and a number of numerical modifications are necessary to achieve good computational accuracy as reported, for example, in BISAR documentation (*9*). However, in this research the use of double exponential (DE) integration together with Richardson extrapolation have proved, as shown in Figures 5 and 6, that the theoretically determined surface responses, e.g. vertical stress and shear stress agree very well with the loading boundary conditions. It may, therefore, be said that computational results with very good accuracy were obtained in this research.

THREE LAYER SYSTEM

A three layered system considered in this research is as shown in Figure 7 on the surface of which there is an action of a vertical load, p, and a horizontal load, q, as shown in Figure 8 and expressed in Equations 1 and 2, respectively. Figure 8(a) shows vertical loads for two cases where ratios between anti-symmetric load and uniformly distributed load are $p_1/p_0 = 0$ and $p_1/p_0 = 1$. Figure 8(b) shows horizontal loads for two cases where ratios

between anti-symmetric load and uniformly distributed load are $q_1/q_0 = 0$ and $q_1/q_0 = 1$. In cases where $p_1/p_0 = 0$ and $q_1/q_0 = 0$, it means uniformly distributed vertical load p_0 and horizontal load q_0, act on the surface of the pavement structure. Furthermore, the value used for p_0 is 0.694MPa, which is the value obtained from an action of a 49kN vertical load uniformly acting on a circular loading plate with radius 15cm. The vertical load p is multiplied by the coefficient of friction μ_f to obtain horizontal load. This means, $q = \mu_f p$. Coefficient of friction may vary depending on the tread pattern of the tire, magnitude of vertical load, dry/wet condition of the road surface, etc. In this regard, an average value of $\mu_f = 0.5$ was used in this research.

Figure 9 shows the variation of σ_x along x-axis due to separate actions of vertical and horizontal loads on the surface of the structure. Figure 9(a) shows the results when the ratios of vertical loads are p_1/p_0 = 0, 1/3, 2/3, 1. $p_1/p_0 = 0$ represents a uniformly distributed load while, p_1/p_0 = 1/3, 2/3 represent trapezoidal load and $p_1/p_0 = 1$ represents triangular load. In case of the action of uniformly distributed load, $p_1/p_0 = 0$, the results show σ_x to be symmetric about $x = 0$ with maximum compressive stress value of 2.18MPa at $x = 0$. As the value of p_1/p_0 increases, position of the maximum compressive stress, σ_x, shifts from $x = 0$ towards the positive x-axis, and for triangular load, where $p_1/p_0 = 1$, the position of maximum compressive stress (σ_x = 2.63MPa) is at $x = 0.08$m. Results show compressive stress for triangular load is about 20% higher than that of uniformly distributed load. Figure 9(b) shows the results of σ_x when the ratios of horizontal loads are q_1/q_0 = 0, 1/3, 2/3, 1. For the case of uniformly distributed horizontal load ($q_1/q_0 = 0$), results show that σ_x is symmetric about $x = 0$ and maximum compressive stress (1.20MPa) is on the positive x-axis and the maximum tensile stress (1.20MPa) is on the negative x-axis. As the values of q_1/q_0 increase, the maximum compressive stress on the positive x-axis increases until it reaches the highest value of 2.11MPa when the load is triangular ($q_1/q_0 = 1$). Consequently, the tensile stress on the negative x-axis decreases until it reaches the lowest value of 0.393MPa when the load is triangular ($q_1/q_0 = 1$).

Figure 10 shows variation of ε_x along the x-axis at the bottom of asphalt concrete layer when vertical or horizontal load is acting on the surface of the structure. In case of the action of uniformly distributed vertical load ($p_1/p_0 = 0$), results show ε_x to be symmetric about $x = 0$ with a maximum tensile strain of 268 μ. As the value of p_1/p_0 increases, there is also an increase in the tensile strain, ε_x, until it reaches the highest value of 332 μ when the load is triangular ($p_1/p_0 = 1$). Furthermore, in case of the action of uniformly distributed horizontal load ($q_1/q_0 = 0$), results show ε_x to be anti-symmetric about $x = 0$, where the maximum compressive strains on the positive and negative x-axis are 41.9 μ. As the value of q_1/q_0 increases, there is an increase in the compressive strain on the positive x-axis and a decrease on the negative x-axis. The maximum and minimum compressive strains of 68.6 μ and 15.4 μ, respectively, were attained when the load was triangular ($q_1/q_0 = 1$).

Figure 11 shows variation of ε_z along the x-axis at the top of the subgrade when vertical or horizontal load is acting on the surface of the structure. In case of the action of

uniformly distributed vertical load ($p_1/p_0 = 0$), results show ε_z to be symmetric about $x = 0$ with a maximum compressive strain of 660 μ. When the load is triangular ($p_1/p_0 = 1$), the maximum compressive strain is 669 μ at x=0.04m, which shows very small influence of the variation of the vertical loading shape. Furthermore, when a uniformly distributed horizontal load ($q_1/q_0 = 0$) is acting, the maximum compressive strain on the positive x-axis and maximum is 38.2 μ. The compressive strain increases to 62.9 μ while the tensile strain decreases to 13.5 μ when the load is triangular ($q_1/q_0 = 1$).

Following the results stated above, effects of triangular vertical and horizontal loads on the variation of responses with depth were investigated and compared. Pavement responses due to horizontal and vertical loads were compared in terms of absolute maximum values. Ratio of responses at the surface of asphalt concrete layer is 2.11/2.63 = 0.80, bottom of asphalt concrete layer is 68.6/332 = 0.21 and top of subgrade layer is 62.9/669 = 0.09, which is an indication that there is a decrease in the responses due to horizontal load as compared to the vertical load. Generally, it is well known that effects of load on a pavement structure decreases with depth. However, if variations of pavement responses due to horizontal and vertical loads were the same, the ratios presented above would also have been the same. The drastic decrease, with depth, in the ratio of responses due to horizontal and vertical load means that the influence of horizontal load is concentrated in the neighborhood of the load application point and decreases drastically with depth.

CONCLUSIONS

Closed form solutions for the case where uniformly distributed vertical and horizontal loads act on the surface of the pavement structure have already been developed by the authors. In the effort to extend application of the multi-layer elastic theory, solutions for trapezoidal load in order to take into consideration action of moment load were developed in this research. This development has made it possible for analysis of a more complex loading condition to be considered and is effective for pavement sections that experience severe loads due to abrupt starting and stopping of vehicle as well as sharp cornering. Moreover, improvement of accuracy for computation of responses at or near the pavement surface has been possible by the application of double exponential integration together with Richardson's extrapolation. The knowledge accrued from this research study may, therefore, be summarized as follows:

Semi-infinity system:

1) In order to investigate computational accuracy of responses at or near the pavement surface, a semi-infinity layer was employed. Analysis for anti-symmetric vertical load (moment load) as well as horizontal load (a product of coefficient of friction, $\mu_f = 0.5$, and vertical load) was performed. Responses at the surface of the semi-infinity layer were found to be very accurate as shown in Figures 5 and 6, which confirms the effectiveness of double exponential integration combined with Richardson's extrapolation.

Three layer system:

2) The triangular load resulted in maximum compressive stress at the surface that was greater by 20% and 70% than results from uniformly distributed vertical load and horizontal load, respectively.

3) Influence of loading shape on strains indicated that, tensile strain, ε_x, at the bottom of the asphalt concrete layer that resulted from triangular load was $332\,\mu$ as compared to $268\,\mu$ from uniformly distributed vertical load, which was an increase by 25%.
4) Influence of shape of horizontal load on strain at the bottom of the asphalt concrete layer indicated that, strain was compressive on the positive x-axis and tensile on the negative x-axis. Uniformly distributed horizontal load resulted in compressive strain of $41.9\,\mu$ while triangular load resulted in compressive strain of from $68.6\,\mu$, which was an increase by 63%. On the other hand, there was a decrease by about 60% on the tensile strain from triangular load as compared to uniformly distribute horizontal load.
5) Variation of the vertical loading shape does not have a significant influence on the compressive strain, ε_z, on the surface of the subgrade. However, in case of horizontal load, triangular load resulted in compressive strain that was 65% higher than that from uniformly distributed horizontal load and tensile strain that was lower by 65% than that from uniformly distributed load.
6) There was a drastic decrease, with depth, in the responses due to horizontal as compared to vertical load, which means that the influence of horizontal load is only limited to areas close to the surface.

Load distribution at the tire/pavement interface is one of the factors that influence pavement surface distresses. Even though it is clear that the load distribution is dependent on the type of tire, the actual distribution for each tire is not yet known. Measured data from Stress-In-Motion (SIM) technology help to develop an understanding of the patterns of contact stress pattern as a function of load. When these types of data are utilized, accurate and practical computation of pavement responses will be achieved. Plans are underway now for research collaboration where the software developed by authors will be used to analyze measured SIM data sets.

ACKNOWLEDGEMENT

In order to compute for responses, Hankel transform is used and it is, generally, difficult to maintain good computational accuracy at or near the surface. Authors would like to take this opportunity to acknowledge very constructive suggestion from Prof. Masatake Mori of Tokyo Denki University in Japan (who is also Professor Emiritus of Kyoto University and former head of the Research Institute for Mathematical Sciences, Kyoto University)

APPENDIX

Struve function, $\mathbf{H}_\nu(z)$, is defined as follows:

$$\mathbf{H}_\nu(z) = \left(\frac{1}{2}z\right)^{\nu+1} \sum_{k=0}^{\infty} \frac{(-1)^k \left(\frac{1}{2}z\right)^{2k}}{\Gamma(k+\frac{3}{2})\Gamma\left(k+\nu+\frac{3}{2}\right)}$$

where if $\nu = 0$: $\mathbf{H}_0(z) = \frac{2}{\pi}\left[z - \frac{z^3}{1^2 \cdot 3^2} + \frac{z^5}{1^2 \cdot 3^2 \cdot 5^2} - \cdots\right]$

Where if $\nu = 1$: $\mathbf{H}_1(z) = \frac{2}{\pi}\left[\frac{z^2}{1^2 \cdot 3} - \frac{z^4}{1^2 \cdot 3^2 \cdot 5} + \frac{z^6}{1^2 \cdot 3^2 \cdot 5^2 \cdot 7} - \cdots\right]$

REFERENCES

1. GAO: Transportation Infrastructure - Highway Pavement Design Guide is Outdated. *Report to the Secretary of Transportation*, November, 1997.
2. Shoukry, S.N. ed. Finite Element for Pavement Analysis and Design. *Proceedings of the First National Symposium on 3D Finite Element Modeling for Pavement Analysis & Design*, Charleston, West Virginia, November 8-10, 1998.
3. Shoukry, S.N. ed. Finite Element for Pavement Analysis and Design. *Proceedings of the Second International Symposium on 3D Finite Element Modeling for Pavement Analysis & Design*, Charleston, West Virginia, October 11-13, 2000.
4. Shoukry, S.N. and T. Scarpas. *3D Finite Element Analysis, Design & Research*, Amsterdam, The Netherlands, 2-4 April, 2002.
5. AASHTO. *A guide for mechanistic-empirical design and analysis*. NCHRP Project 1-37A. http://www.trb.org/mepdg/home.htm. Washington, USA. 2004.
6. Soon, S-C., A. Drescher, and H. K. Stolarski. Tire-Induced Surface Stresses in Flexible Pavements, *Transportation Research Records*, No. 1896, 2004, pp.170-176.
7. Nishizawa, T. Development of Package for Analysis of Concrete Pavement Based on 3Dimensional Finite Element Method. *Journal of Pavement Engineering, JSCE, Vol. 5*, 2002, pp.115-124. (in Japanese)
8. Maina, J. W. and K. Matsui. Developing software for elastic analysis of pavement structure responses to vertical and horizontal surface loadings, *Transportation Research Records*, No. 1896, 2004, pp.55-66.
9. De Jong, D. L., M. G. F. Peutz, and A. R. Korswagen. Computer Program BISAR, Layered systems under normal and tangential loads. *External Report AMSR.0006.73*, Koninklijke/Shell-Laboratorium, Amsterdam, 1979.
10. Matsui, K., J.W. Maina, and T. Inoue. Axi-symmetric Analysis of Elastic Multilayer System Considering Interface Slips. *International Journal of Pavements*, Vol. 1 No. 1, January 2002, pp. 55-66.
11. De Beer, M., C. Fisher, L. Kannemeyer. Tyre-pavement interface contact stresses on flexible pavements - quo vadis?. Roads - *The Arteries of Africa; 8th Conference on Asphalt Pavements for Southern Africa (CAPSA '04)*, Sun City, North West Province, South Africa, September 12-16, 2004, pp. 681-702.
12. De Beer, M., C. Fisher, L. Kannemeyer. Towards the Application of Stress-In-Motion (SIM) Results in Pavement Design and Infrastructure Protection. *8th International Symposium on Heavy Vehicle Weights and Dimensions (8ISHVWD)*. Misty Hills Country House & Conference Centre, Muldersdrift, South Africa. March 14-18, 2004.
13. Maina, J. W., K. Fujinami, K. Matsui, and T. Inoue. Pavement Response due to Torsional Surface Loading. *Seventh International Conference the Bearing Capacity of Roads, Railways and Airfields* (in CD-ROM), NTNU, Trondheim, Norway, June 27-28, 2005.
14. Mori, M. *Fortran77 Programming for Numerical Computations* (revised edition), Iwanami Shoten. 2000.4.
15. Ooura,T. and M. Mori. The Double Exponential Formula for Oscillatory Functions over Half Infinity Integral, *Journal of Computational and Applied Mathematics 38*, 1991, pp.353-360.

LIST OF FIGURES

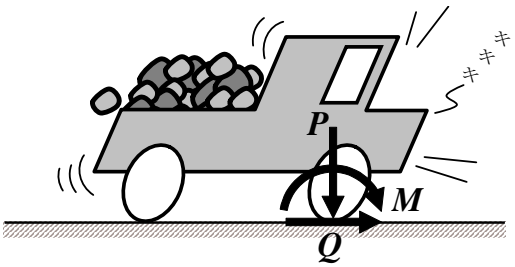

(a) Hypothetical tire loading

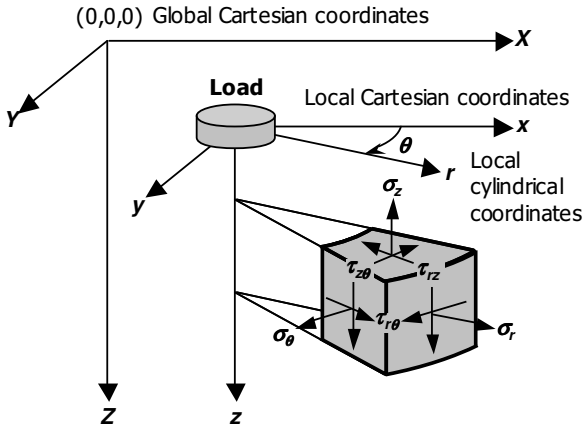

(b) Direction of positive normal and shear stresses on infinitesimal cube

FIGURE 1 Pavement surface loading and positive normal and shear stresses.

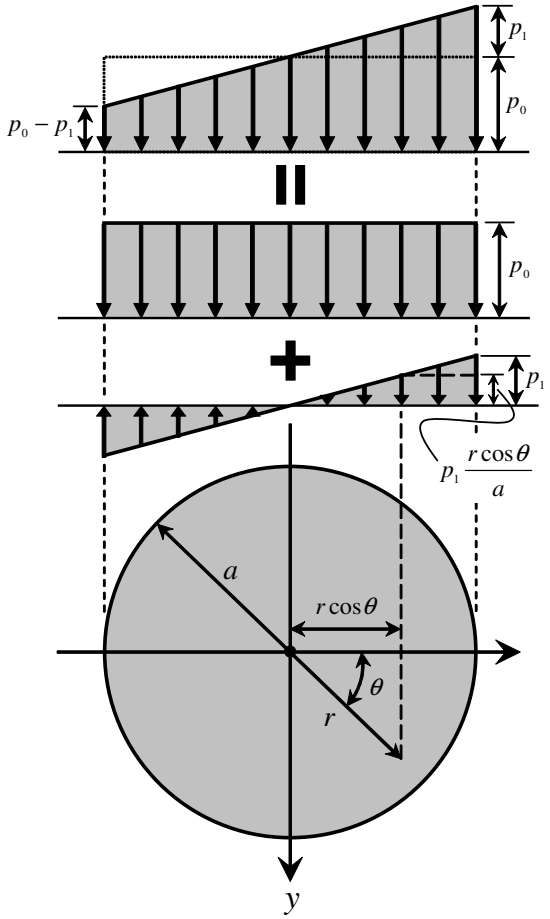

FIGURE 2 Pavement surface moment loading distribution.

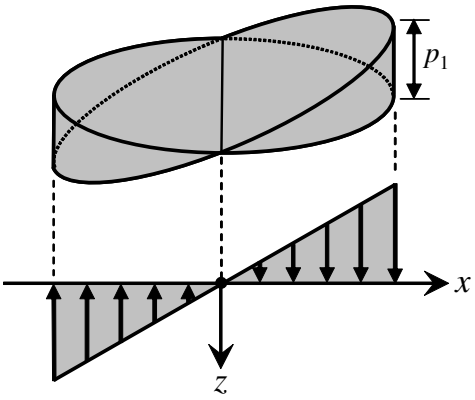

FIGURE 3 Vertical moment loading.

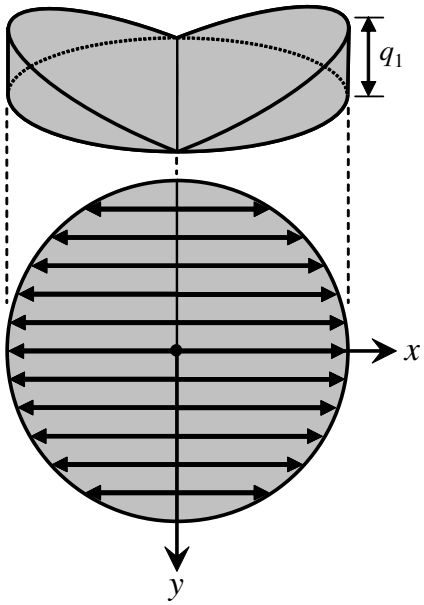

FIGURE 4 Horizontal moment loading.

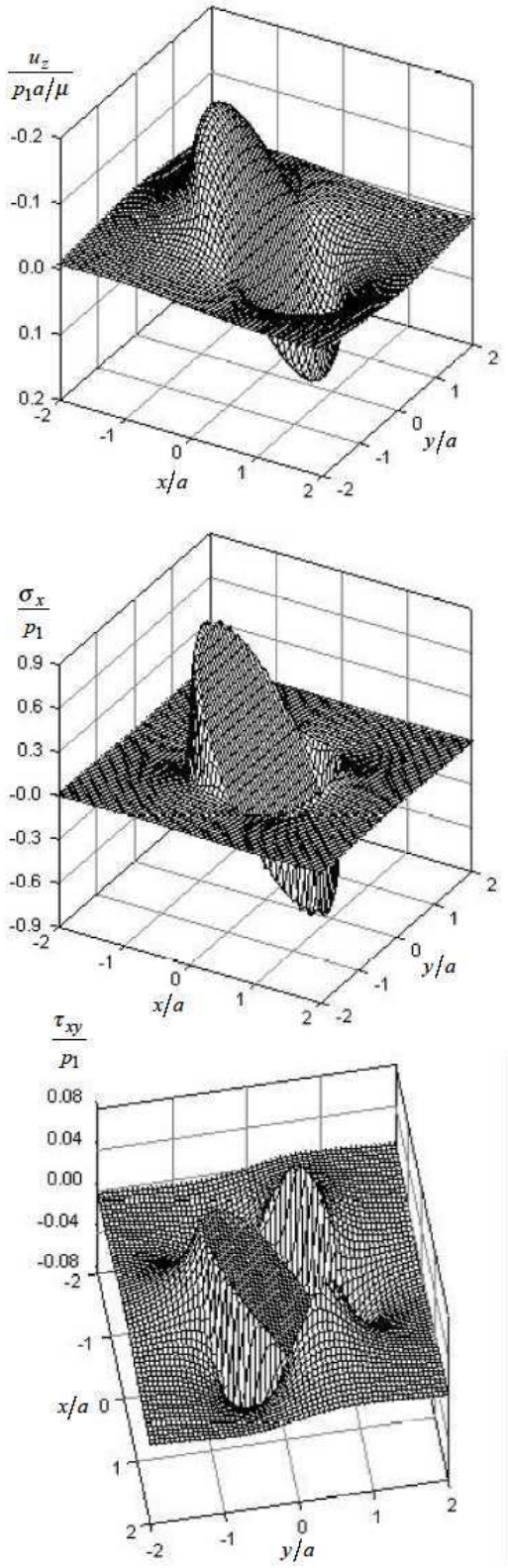

FIGURE 5 Displacement and stresses due to vertical moment loading.

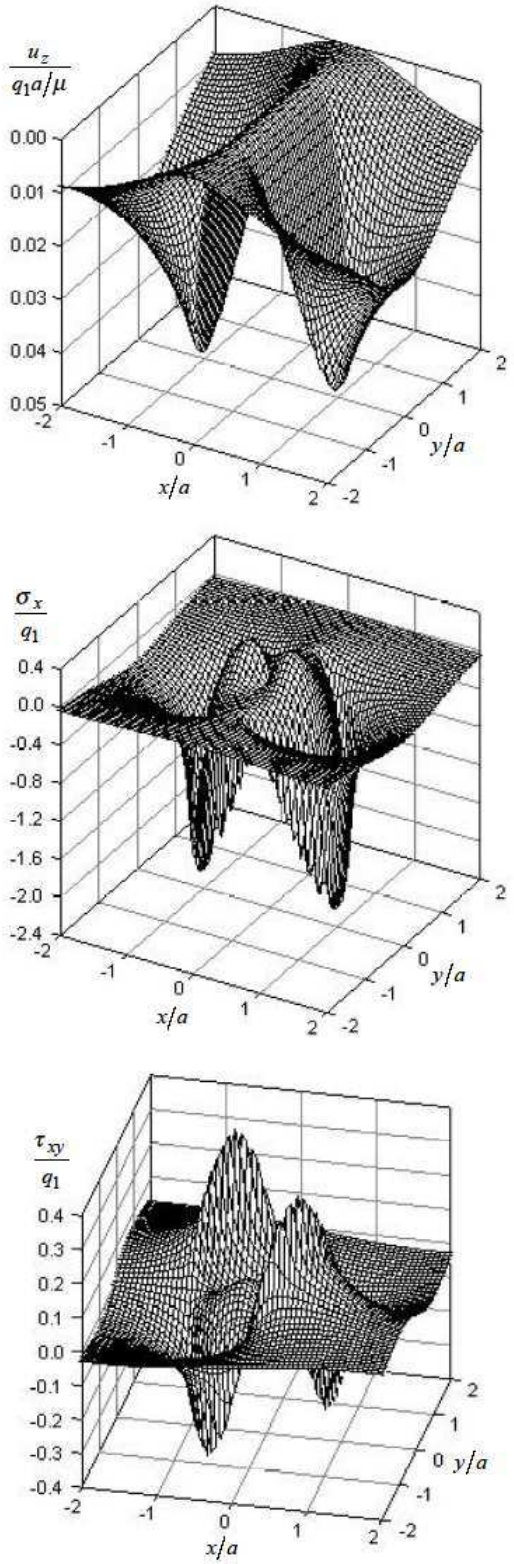

FIGURE 6 Displacement and stresses due to horizontal moment loading.

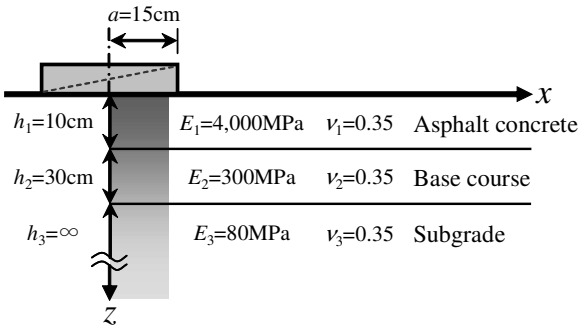

FIGURE 7 Three layer model.

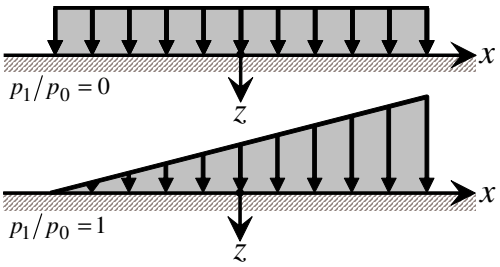

(a) vertical loading

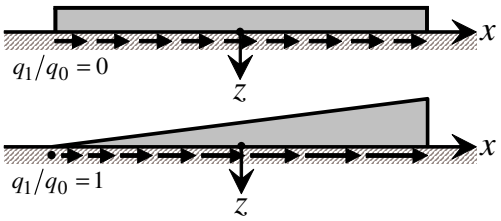

(b) horizontal loading

FIGURE 8 Pavement surface loading distribution.

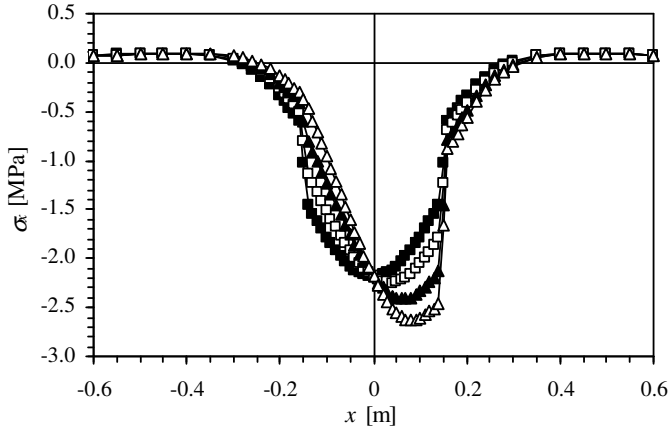

(a) stress due to vertical loading

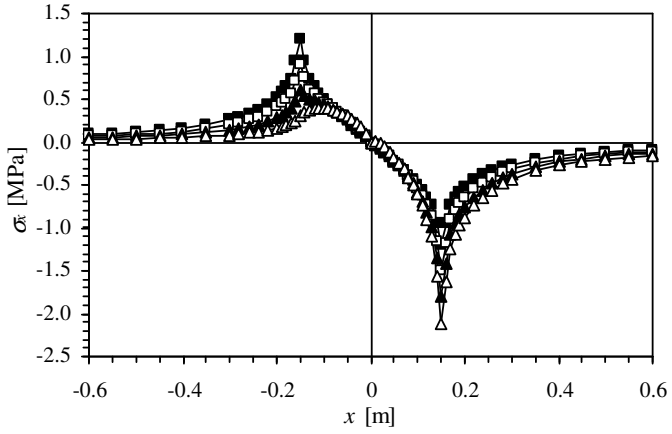

(b) stress due to horizontal loading

FIGURE 9 Distribution of pavement surface stress, σ_x.

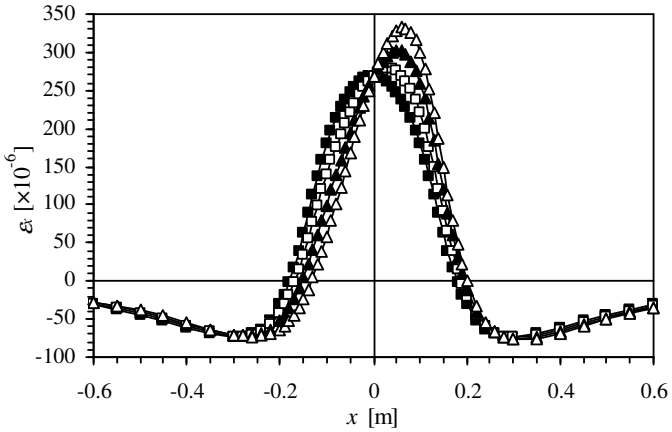

(a) strain due to vertical loading

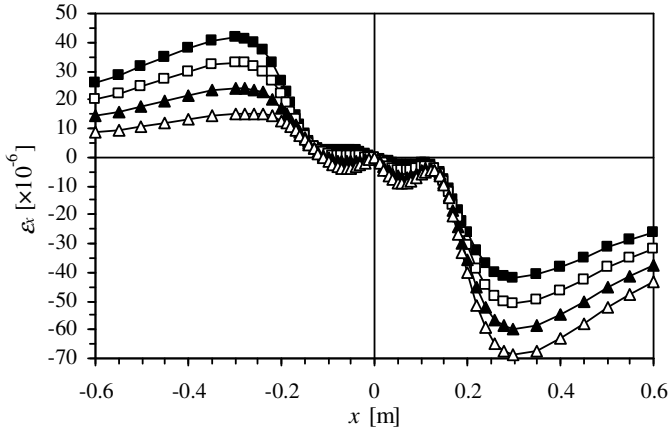

(a) strain due to horizontal loading

FIGURE 10 Distribution of strain, ε_x, at the bottom of asphalt concrete layer.

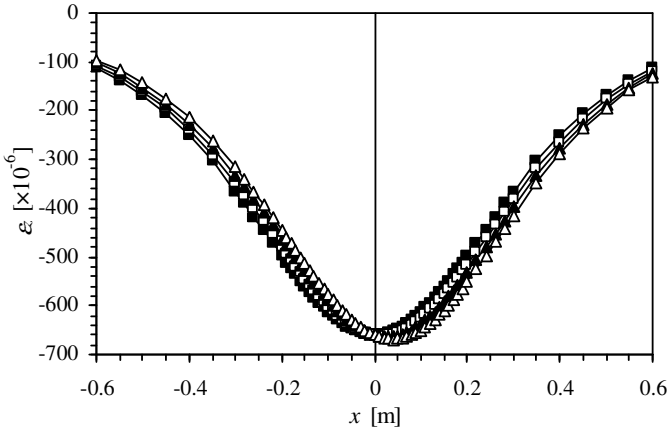

(a) strain due to vertical loading

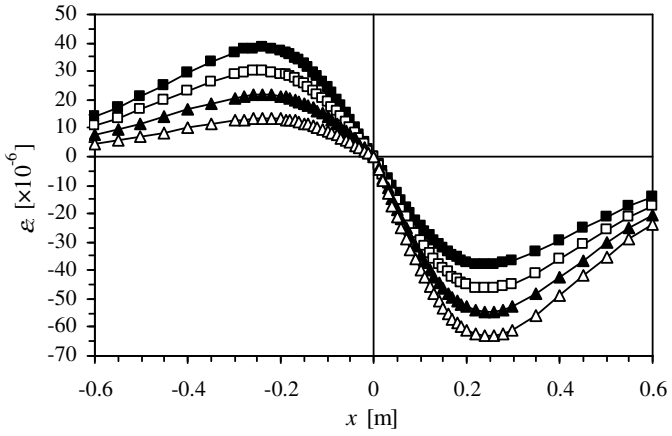

(b) strain due to horizontal loading

FIGURE 11 Distribution of strain, ε_z, at the top of subgrade layer.